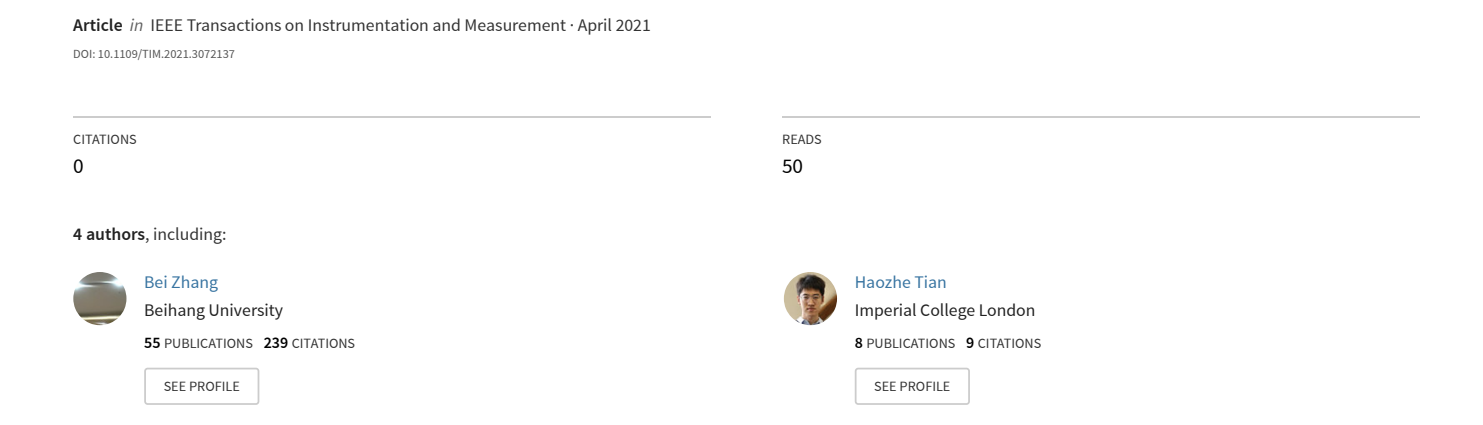
Instrumentation of Surface Plasmon Microscopy: Complete Scheme of Signal Extractions



TIM-20-02451

Instrumentation of surface plasmon microscopy: complete scheme of signal extractions

Bei Zhang, Member, IEEE, Haozhe Tian, Tianyu Xiao, and Jing Zhang

Abstract—Objective-coupled surface plasmon microscopy (SPM) features on both extremely high sensitivity and high resolution. However, this promising system is still operated in labs without commercial instrument. One big challenge is how to extract and classify the plasmonic signals from batches of experimentally acquired back focal plane (BFP) images accurately and automatically. To solve this problem, this work presents a complete solution for the first time which significantly promotes the application and instrumentation of BFP typed SPM in two aspects: 1) It utilizes an object detection model to pre-determine the classification and raw localization of plasmonic absorption profiles for the convenience of subsequent fine detection. 2) It utilizes self-correlation to identify the plasmonic signal more accurately; When the mode of plasmonic signal is determined, the self-correlation procedure can operate independently, with faster speed and wider applicability than our previously proposed Fourier correlation analysis. The whole scheme is experimentally verified on our home-developed SPM. And the performance of the proposed scheme is illustrated through comparisons with other approaches.

Index Terms—Surface plasmon microscopy, Back focal plane, Identification, Classification, Object detection, Self-correlation

I. INTRODUCTION

Surface plasmon (SP) is an oscillation of delocalized electrons between the metal-dielectric interface. It is extremely sensitive to surface properties and has great potential in bio-sensing [1, 2]. Current SP configuration falls into two categories: prism-coupled (Fig. 1(a)) and objective-coupled (Fig.1 (b)). Prism-coupled SP configuration has extremely high sensitivity but suffers relatively low lateral resolution due to the lateral propagation of SPs [3]. Objective-coupled configuration localizes SPs into a region comparable to diffraction limit and further increases the measurement accuracy. With similar configuration to conventional optical microscopy, it is also given the name of surface plasmon microscopy (SPM).

So far, various types of SPM have been invented, including linear and radial polarization mode [3, 4], scanning and widefield mode [5-8], intensity and phase mode [4, 9], back focal plane (BFP) and our previously proposed confocal mode [10, 11], etc. However, most of the existing commercial configurations are prism-coupled configurations. The latter objective-coupled SPMs are still operated in labs and no commercial instruments have been reported, even for the

simplest BFP-typed SPM (Fig. 1(b)). The main challenge is how to extract and classify the plasmonic signals from batches of experimentally acquired BFP images accurately and automatically.

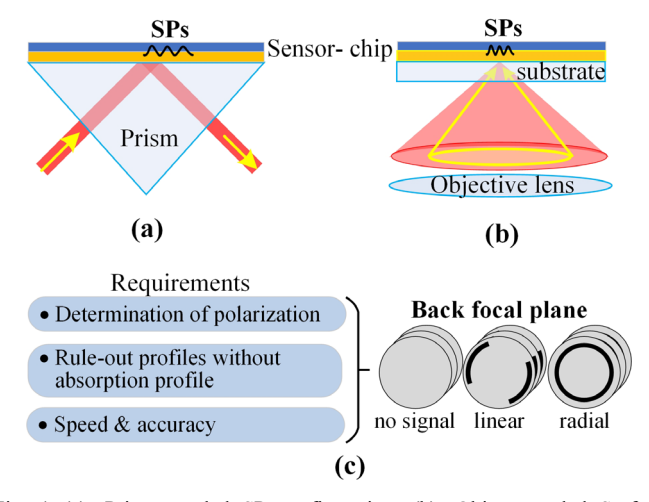


Fig. 1 (a). Prism-coupled SP configuration. (b). Object-coupled Surface plasmon microscopy. (c). Requirements on BFP profile identification.

Currently, there are generally three solutions to identify BFP images: i) 1-D identification, which gives relatively rough identification results; ii) morphology [11], which is generally applicable to the case of low coherence noises and concentricity between the absorption profile and the clear aperture; iii) our previously proposed Fourier correlation analysis (FCA) [12]. 1-D identification and morphology do not operate well on experimentally acquired images with heavy noise. Our previously proposed FCA solved this problem since it minimized the influence of random noise and maximized the symmetric pattern on the BFP. However, even if the influences of coherent noises are ignored, there are still two issues to be solved: 1) Previous identification approaches are based on the strict pre-assumption that all the acquired BFP images contain obvious absorption profiles with pre-known mode of polarization. This condition is hard to fulfill in practice, especially when loads of BFP images are to be identified. 2) The FCA algorithm may become inapplicable when the SP profile is in linear mode. It is inevitable to solve the above two issues in a complete solution to identification of BFP images.

This work is to propose a complete identification scheme to

The study was funded by Fundamental Research Funds for Central Universities of China (YWF-21-BJ-J-715).

The authors are with the Department of Automation Science and Electrical Engineering, Beihang University, Beijing, 100191, China. (Email:

bei.zhang@buaa.edu.cn, zhangjing@buaa.edu.cn) 17376184@buaa.edu.cn, xt

<u>xty_15@163.com</u>,

solve the two issues in BFP typed SPM above.

For the first issue, the polarization modes of absorption profiles need to be pre-determined, and BFP images with no plasmonic signals need to be ruled out. Fundamentally, both of these requirements refer to the identification of absorption profiles. Present works propose an object detection model to solve the issue [13]. Object detection models bring two benefits to the proposed identification scheme: firstly, it functions for identification, which allows the pre-determination of polarization mode and the rule-out of BFP images with no plasmonic signals; secondly, it functions for the localization of the absorption profile which helps to determine the region of interest on BFP images and thus reduce computational cost of later procedures.

Here the selection of specific object detection model for the proposed BFP images identification scheme is explained. There are two stages of object detection models: conventional machine-learning based (utilizing hand-crafted features), and deep-learning based (utilizing learned features) [13]. The present work selects the latter deep-learning based models for two reasons. Firstly, the deep-learning based object detection models far surpass conventional models in terms of accuracy [13, 14]. Secondly, the deep-learning based Object detection models operate without hand-crafted features [13], which suits application in BFP typed SPM for its easy configuration. One may concern that the training of deep-learning based object detection model is slower and more complicated. Actually, this is not a problem for its application in BFP typed SPM. Firstly, the object detection model only needs to be trained once during configuration. For the experiment stage of identification, the current object detection models, such as Faster Region-Convolution Neural Network (Faster R-CNN) [15] and Single Shot MultiBox Detector (SSD) [16], are fast enough to achieve real-time performance. Secondly, methods such as transfer learning can be used to make these deep networks easier to train. Therefore, the present work selects deep-learning based models for their high accuracy, easy feature extraction, and fast identification speed. It is worth noting that the object detection model in this work is a trial and mainly aims to verify the proposed complete identification scheme. In future works, other specific models can also be applied for the identification of BFP images.

For the second issue, a general solution for identifying absorption profiles in both linear and radial polarization modes is needed. To solve this issue, the algorithm of self-correlation is proposed. To the best of the authors' knowledge, it is the first time to propose the algorithm of self-correlation in SP absorption profiles. Different from the previously utilized Fourier correlation analysis (FCA) which works for BFP images with radial polarization mode, but only partially works for BFP images with linear polarization mode (FCA loses effect when the linear absorption profiles are in a certain position), the present self-correlation can perfectly work for both of the two polarization modes with no specific conditions required. Furthermore, the present self-correlation solution provides a faster operating speed, which is significantly important for real-time measurement. A quantitative comparison of FCA and self-

correlation will be given in part 'V.Discussion'.

The complete BFP images identification scheme is experimentally verified on our home-developed SPM. And the performance of the proposed scheme is illustrated through a comparison with previous BFP identification approaches. To the best of our knowledge, this is the first time to present a complete and automatic plasmonic signal extraction and classification scheme, which promotes the application and implementation of BFP typed SPM significantly.

II. PRINCIPLE AND METHODOLOGY

SPM reflects the surface property of plasmonic sample by the excitation angle of SPs. In BFP typed SPM, the excitation angle of SPs is measured according to the locations of SP profile and clear aperture (CA). When the illuminant is in linear or radial mode, the SP profile on the reflected BFP appears as a pair of crescents or a complete circle [11]. Fig. 2 shows the principle of the proposed identification solution. It mainly contains two parts: A. classification of BFP images and raw localization of profiles, and B. fine detection of SP and CA profiles. The object detection model of Faster R-CNN and the algorithm of self-correlation are responsible for the two part respectively.

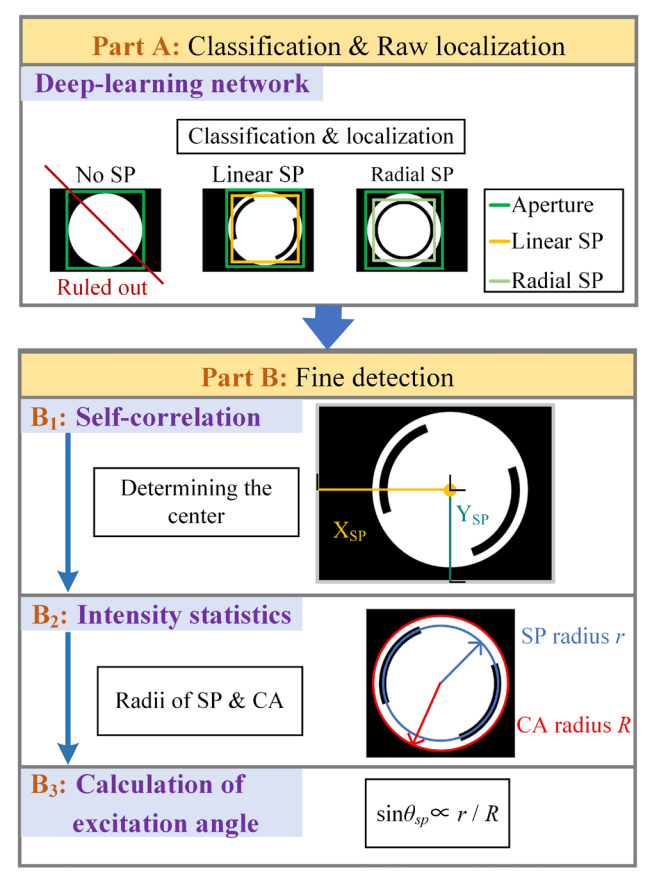


Fig. 2. Principle of the proposed identification solution. Part A: classification and raw localization of SP and CA profiles using Faster R-CNN. Part B: B_1 . Center-detection using self-correlation. B_2 . Radii measurement using intensity statistics. B_3 . Calculation of excitation angle.

Part A. Classification and Raw Localization

As mentioned before, there are generally three categories of BFP images: image with no SP profile, image with linear SP

profile, and image with radial SP profile. Before precise location of the SP and CA profiles, the classification and raw localization of SP profiles should be performed in advance. In this work, the Faster R-CNN is utilized to accomplish this task [15]. The principle of Faster R-CNN is shown in Fig. 3. It can generally be divided into two stages. In stage 1, Faster R-CNN uses a neural network called region proposal network (RPN) to roughly localize SP and CA profiles in the form of boundingboxes [15]. In stage 2, profiles localized in stage 1 are classified into the three categories mentioned above. In particular, the images with no SP profile are taken as singularities and ruled out in subsequent procedure. In the meanwhile, stage 2 of Faster R-CNN also amends the localization result generated in stage 1 for convenience of subsequent identification. Readers can refer to [15] for more technical details. And the reasons for choosing Faster R-CNN are given in the discussion in Section IV.

Localization and classification by Faster R-CNN provides great convenience for subsequent identification of SP and CA profiles. However, although the approximate radii of SP and CA are given by localization of Faster R-CNN, they are not accurate enough. There are mainly two reasons for error in radii given by Faster R-CNN: First, the structure of Faster R-CNN determines that it only generates numerical solutions which are approximations of the radii. Second, training of Faster R-CNN might introduce error. Faster R-CNN is trained by a manually marked training set. The manual marking process totally depends on human eyes and induces errors more or less. Besides, the training of network might be insufficient to find the optimal coefficients due to slight overfitting or underfitting. Both the two kinds of errors are inevitable in most of object detection networks. Therefore, fine detection based on selfcorrelation and intensity statistics is proposed to accurately measure the radii of SP and CA.

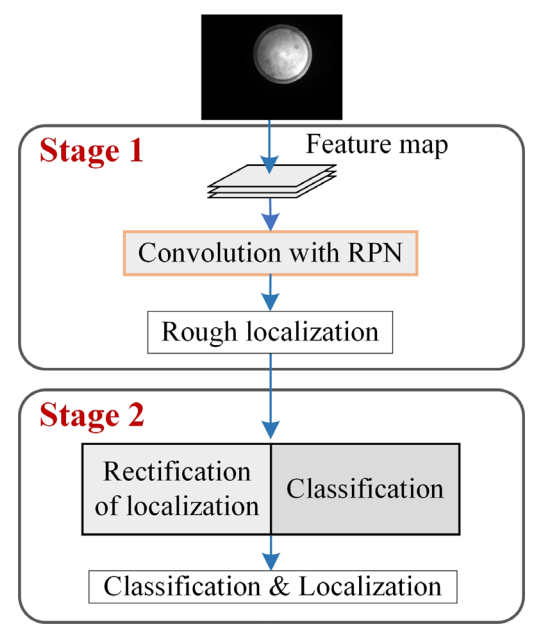


Fig. 3. Schematic drawing of Faster R-CNN. Faster R-CNN is a two-stage object-detection network that is able to classify and localize target object (SP and CA profiles in this work). Stage 1 is to use RPN to localize SP and CA profiles roughly. Stage 2 is to rectify localization generated in stage 1 and classify the SP profiles.

Part B. Fine Detection

The procedure of fine detection of SP and CA profiles is shown in Fig. 4. It contains three main steps: (B_1) using self-correlation to identify the center of BFP; (B_2) using intensity statistics to determine SP and CA profiles and measure their radii; (B_3) using radii of SP and CA to calculate excitation angle. The detailed process is illustrated as follows.

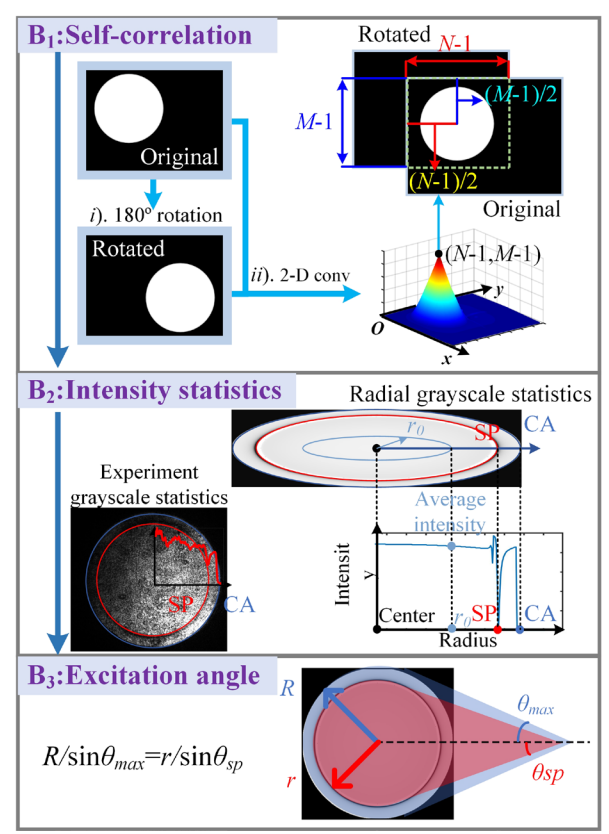


Fig. 4. Process of fine detection. B1: 2-D convolution is performed between the BFP images before and after a rotation of 180°. The profile center is determined according to the maximum of the convolution. B2: Determine the radii of SP and CA profiles by radial intensity statistics. Intensity statistics curve is obtained by calculating average intensity of circles with radius r_0 in range $[0, R_{up}]$ (R_{up} is a radius bigger than the radius of CA profile). SP and CA are identified on the intensity statistics curve. B3: Calculate the excitation angle.

(B₁) Self-correlation

SP and CA profiles are both center symmetric patterns. Self-correlation which maximizes the symmetric pattern and minimizes the random noise on the BFP image [12, 17] is utilized to detect the centers of the two profiles. Procedures of self-correlation is shown in Fig. 4(B₁). First, the original BFP image is rotated by 180°. Second, the 2-D convolution between the origin BFP image and the rotated image is calculated according to the following equation:

$$g(n,m) = \sum_{x=0}^{w-1} \sum_{y=0}^{h-1} f(x,y) \cdot f(n-x,m-y)$$
 (1)

The value of 2-D convolution reflects the level of coincidence of the original image with the rotated image. Since both SP and CA profiles are center symmetric profiles (SP and CA), the BFP has little change before and after the rotation of 180°. And the maximum value of 2-D convolution occurs when the center of original image coincides with that of the rotated image.

Supposing the maximum occurs at the position of (N, M), the profile center (x_{center}, y_{center}) is:

$$\begin{cases} x_{center} = \frac{N-1}{2} \\ y_{center} = \frac{M-1}{2} \end{cases}$$
 (2)

According to property of convolution in spatial domain, one can also calculate the self-correlation by two-dimensional Fourier transformation.

$$g(n,m) = F^{-1} \{ F[f(x,y)] \cdot F[f(x,y)] \}$$
 (3)

Equation (3) is actually a circular convolution, which generates multiple solutions and thus requires priori knowledge of BFP profile location. For simplification, (1) is used in this work to calculate self-correlation.

(B₂) Intensity Statistics

The schematic diagram of intensity statistics is shown in Fig. 4(B₂). Intensity statistics operates on the center determined by self-correlation. First, intensity statistics curve is obtained from BFP images. Consider radius r_0 in range $[0,R_{up}]$ (R_{up} is a radius bigger than the radius of CA profile). For a certain r_0 , average intensity of pixels with a distance of r_0 from the center is calculated. Since the calculation takes a ring of pixels into account, effect of random noises is removed. By calculating average intensity for r_0 in range $[0,R_{up}]$, an intensity statistics curve is obtained. Intensity statistics curve of a schematic BFP image is shown in Fig. $4(B_2)$. The horizontal axis of the curve is radius and the vertical axis of the curve is intensity. Second, the radii of SP and CA profile are identified based on the intensity statistics curve. The radius of SP profile r is located at the radius with minimum intensity (marked by the red point) and the radius of CA profile R is located at the radius with the minimum difference (marked by the blue point).

(B₃) Calculation of excitation angle

In BFP-typed SPM, the relationship between the excitation angle of SPs θ_{sp} and the maximum focusing angle θ_{max} is characterized by Abbe's sine condition:

$$r / \sin \theta_{sp} = R / \sin \theta_{max} \tag{4}$$

where r is the radius of SP, R is the radius of CA profile. For a given system, the sine of the maximum focusing angle is determined according to the numerical aperture (NA) and refractive index of immersion medium n of the objective lens:

$$\sin \theta_{\text{max}} = NA/n \tag{5}$$

By substituting Eq. 5 into Eq. 4, the excitation angle θ_{sp} can be calculated by:

$$\theta_{sp} = \arcsin\left(\frac{NA}{n} \cdot \frac{r}{R}\right) \tag{6}$$

Here the measurement process is accomplished.

III. CONFIGURATION

A. Experiment configuration

A surface plasmon microscopy (SPM) system is configured to obtain BFP images. The polarization mode is controlled to

obtain both the BFP images of both linear and radial modes. And the tested samples are prepared to obtain both BFP images with and without the absorption profiles. Fig. 5 shows the details of experiment configuration. Fig. 5(a) gives the schematic diagram of optical arrangement. A laser is utilized as illumination. After collimated and expanded by a beam expander, the incident beam was then focused on the plasmonic sample by an oil-immersion objective lens. And the conjugate plane of the reflected BFP is finally imaged by lens 3 and lens 4 and recorded by the CCD camera. Fig. 5(b) shows the practical experiment configuration. A He-Ne laser with a wavelength of 632.8nm is utilized as the illumination source. An 100X oil-immersion objective lens with a NA of 1.25 (@Olympus) is utilized to excite the plasmonic signal. Considering that the reference tube length of the objective by Olympus is 160mm, the corresponding focal length of the objective is given by 160/100=1.6mm. As a result, the corresponding diameter of the CA is 2fNA, which is 4mm in this case. The beam waist of the applied He-Ne laser is 0.8mm and a 5X of beam expander is applicable. However, to obtain a more uniform illumination, a 10X beam expander is utilized in our experiment system. The tested samples are mounted above the objective lens (See the blue block in Fig. 5(b)). The detailed structure of the multi-layer sample is enlarged on the right side of Fig. 5(b) for clear illustration. It utilizes the classical sandwiched structure and consists of 1nm Ti, 46nm Au, and 5/10/15nm MgO. A Charge Coupled Device (CCD) with the pixel size of 3.75µm and resolution of 968×1024 is utilized to image the BFP which gives the CA and SP signals. To acquired BFP images which takes sufficient pixels on the CCD detector, the actual BFP of the objective is shrunk by 2.67 times by the Lens 3 (f=200mm) and Lens 4 (f=75mm). Fig. 5(c) shows the recorded BFP images in three categories: with no SP profile, with linear SP profile, and with radial SP profile.

B. Construction of object detection model

In this work, the Faster R-CNN is utilized to implement the classification and raw localization of BFP images. The construction procedure of the Faster R-CNN model is demonstrated in Fig. 6(a), which contains three steps: 1) creation of dataset, 2) training of Faster R-CNN, and 3) evaluation of Faster R-CNN.

1) Creation of dataset

BFP images obtained on our home-developed SPM are used as the original dataset, based on which a validation set and a train set are created. The procedure of dataset creation is shown in Step 1 of Fig. 6, which mainly contains three operations.

Firstly, BFP images are acquired from our home-developed BFP-typed SPM. Images with severe noise are discarded. The rest of the images with obvious profiles are manually classified into three classes: no SP, linear SP, and radial SP.

Secondly, a validation set is created. More specifically, the validation set consists of 1000 pieces of randomly selected images from the three categories of original BFP images, on which the bounding boxes of SP and CA profiles are manually marked (the squares on BFP images in Fig. 6 Step 1). Each side

of the bounding box is tangent to the SP or CA profile and is considered to be error free. And half of the length of the manually marked bounding boxes are later considered as the ground-truth of the radii of SP and CA profiles r_{tru} and R_{tru} . The two parameters are involved in later evaluation of Faster R-CNN. This validation set is only created for hyper-parameter tuning and evaluation of the training Faster R-CNN model. For complete evaluation of the proposed identification scheme, BFP Images (test set) that are not involved in the training of Faster R-CNN will be used. Detailed evaluation of the complete identification scheme is in section 'IV. Experimentation'.

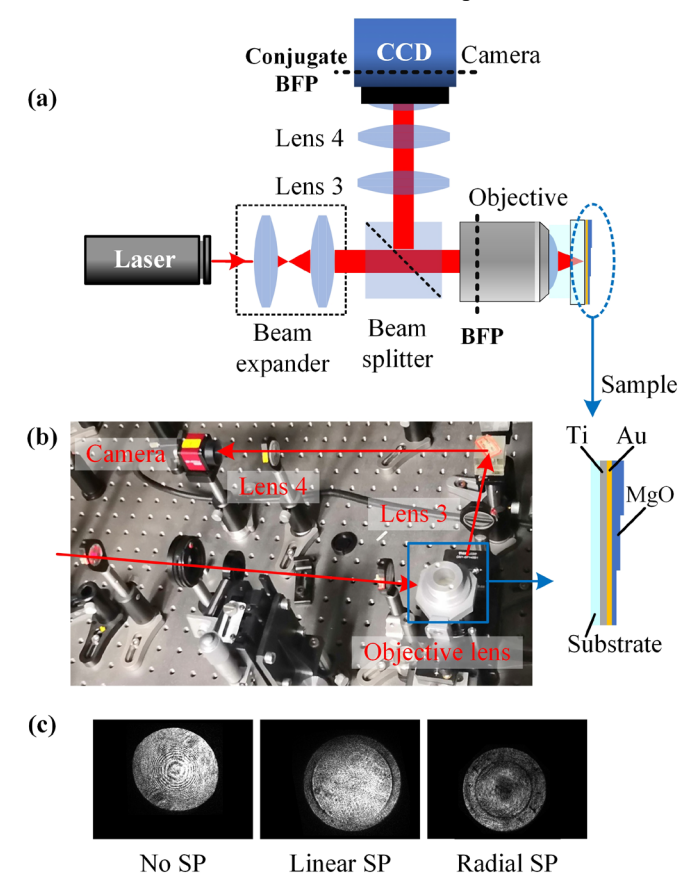


Fig. 5. Experiment configuration. (a) Schematic diagram of optical arrangement. (b) Experimental configuration (He-Ne laser with a wavelength of 632.8nm and 1.25NA objective lens) and structure of the multi-layer sample (1nm Ti, 46nm Au, and 5/10/15nm MgO). (c) Three categories of recorded BFP images.

Thirdly, a train set is created to train Faster R-CNN. In the training process, the Faster R-CNN model might overfit data when the train set is too small. In order to attenuate overfitting, the original BFP images are augmented. During data augmentation, new images are generated from experimentally obtained images. Data augmentation in this work involves several operations: 1) random cropping, 2) random mirroring, 3) random rotation, 4) random adjustment of brightness, and 5) random adjustment of contrast. Random cropping means the generated images will be cropped into smaller images containing SP profiles and then reshaped into their original size. Random mirroring means the generated images has 33.3% chance to be mirrored along the y-axis. Random rotation means the

generated image will be randomly rotated and then cropped and reshaped into their original size. Random adjustment of brightness means the contrast of the generated images will change between the value of 32 and 255. Random adjustment of contrast means the contrast of the generated images will change between the value of 0.5 and 1.5. For the detailed realization of these operations, readers can refer to the official TensorFlow document of data augmentation functions [18].

After augmentation, the images are manually marked with bounding boxes, which serves as the ground truth to train the localization ability of Faster R-CNN. The number of augmented images is related to the amount and quality of the original images. Generating a large number of images would increase the accuracy of Faster R-CNN, but also result in a long training time. The Faster R-CNN exhibits adequate identification accuracy on the validation set when the original images are augmented to 5000 images.

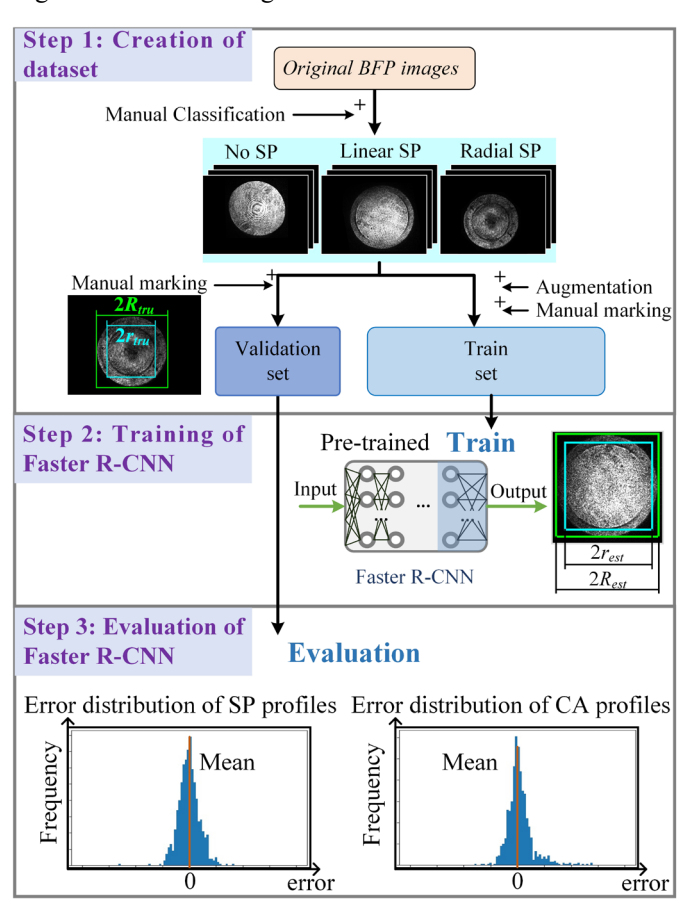


Fig. 6. Construction of Faster R-CNN. Step 1: creation of dataset. Step 2: training of Faster R-CNN and the output image of well-trained Faster R-CNN. Step 3: evaluation of Faster R-CNN.

2) Training of Faster R-CNN

Faster R-CNN is made up of many layers and each layer have many coefficients. To implement the function of SP and CA profiles identification and classification, one needs to train the network and update these coefficients. Training all the layers of Faster R-CNN is extremely time-consuming. Here we apply the transfer learning which is to train the last few layers of a pre-trained model [19]. A pre-trained Faster R-CNN model [20] from the TensorFlow 1 Detection Model Zoo is utilized in

this work. Fig. 6 Step 2 shows a schematic drawing of the Faster R-CNN model. The model is based on inception-v2 and is trained with the COCO dataset. For details of this model (training data, number of layers, etc.) readers can refer to [20, 21]. The train set created above is applied to this model to train its ability to identify SP and CA profiles. Gradient descent with momentum is used for optimization. TABLE I lists the training configurations applied in transfer learning.

TABLE I
TRAINING CONFIGURATIONS

Configuration	Value
Batch size	4
Initial <i>Lr</i>	0.001
Lr after 20000 iterations	0.0001
Lr after 50000 iterations	0.00001
Momentum	0.9
Maximum number of iterations	100000

Lr is the abbreviation of learning rate.

3) Evaluation of Faster R-CNN

The Faster R-CNN is evaluated with the validation set (ground-truth). After training, the network is capable of automatically generating bounding boxes of SP and CA profiles. Half the length of the automatically marked bounding boxes are taken as the estimated radii of SP and CA profiles r_{est} and R_{est} respectively. These two parameters are involved in later evaluation of Faster R-CNN.

Two aspects are considered in the evaluation process: *i*) accuracy of classification and localization, *ii*) accuracy of size measurement.

- i) The accuracy of classification and localization is evaluated by the terms Average Precision (AP) and mean Average Precision (mAP), both of which are numbers range from zero to unity. AP is a widely utilized metric in object detection, which is positively related to the identification accuracy. Identification of each categories of profiles generates an AP. Readers can refer to [22] for more details on definition and calculation process of AP. As for the term mAP, it reflects the overall performance of the object detection model and is defined as the arithmetic mean of the APs of CA, linear SP, and radial SP profiles. TABLE II shows the AP and mAP of Faster R-CNN on validation set. Both of them are close to unity, which indicates the high accuracy of the trained network.
- ii) The accuracy of size measurement is evaluated by the term confidence interval, which denotes the range where the measured profile size locates with a certain probability. Similarly, the confidence interval is evaluated with the validation set to Faster R-CNN. TABLE III lists notations and the corresponding explanations involved in determination of confidence interval.

Step 3 in Fig. 6 shows the measurement error of SP profiles e_r and CA profiles e_R . Both of them can be regarded as normal distributions according to the central limit theorem. The mean values and standard deviations of the two distributions are calculated and the results are listed in TABLE IV. Since standard deviations of error distribution of e_r and e_R equal to

those of r_{est} and R_{est} , SP and CA profiles locates in the regions of $r_{est} \pm 3\sigma_r$ and $R_{est} \pm 3\sigma_R$ with a probability of 99.74% respectively. In the later fine detection, the accurate radii of SP and CA profiles are determined in the corresponding regions to reduce computational cost.

TABLE II

AP AND MAP OF IDENTIFICATION

AP of CA profile	AP of linear SP profile	AP of radial SP profile	mAP
0.9991	0.9994	0.9996	0.9994

TABLE III NOTATIONS

Notations	Explanations
r _{tru}	Ground truth of SP radius (manually marked)
R_{tru}	Ground truth of CA radius (manually marked)
rest	Estimated SP radius by Faster R-CNN
R_{est}	Estimated CA radius by Faster R-CNN
e_r	Error of SP radius estimation (r _{est} minus r _{tru})
e_R	Error of CA radius estimation (Rest minus Rtru)
μ_r	Mean value of e_r
μ_R	Mean value of e_R
σ_r	Standard deviation of e_r
σ_R	Standard deviation of e_R

Radius equals to half the length of bounding box. r_{tru} and R_{tru} are calculated from manually marked bounding boxes (Step 1 of Fig. 6). r_{est} and R_{est} are calculated from bounding boxes generated by Faster R-CNN (Step 2 of Fig. 6). e_r equals to r_{est} minus r_{tru} . e_R equals to R_{est} minus R_{tru} .

 $\label{thm:table_iv} \textbf{TABLE IV} \\ \textbf{MEAN VALUE AND STANDARD DEVIATION OF SPS AND CAS}$

	Value
μ_r	9.9×10 ⁻⁵
σ_r	2.5×10^{-3}
μ_R	4.2×10 ⁻⁴
σ_R	2.3×10 ⁻³

IV. EXPERIMENTATION

To test the complete identification scheme, the proposed solution is applied to the identification of SP and CA profiles on BFP images captured with our home-developed SPM (test set). These captured images are neither in the train set nor the validation set.

Part A. Classification and Raw Localization

The well-trained Faster R-CNN classifies the BFP images and marks bounding boxes of SP and CA profiles automatically. BFP images with no SP signal are ruled out in the meanwhile. Since the SP and CA profiles only take up a small part of the whole image, the Faster R-CNN further crop the whole image into a smaller region of interest (RoI), whose length is actually 20 pixels larger than the length of the bounding box of CA. Fig. 7(a) shows some identification results and the cropped RoIs of the Faster R-CNN. By running later procedures only in the cropped RoIs, identification speed is increased with less data to be processed. The accuracy of identification is also improved because noise in the background is removed.

Part B. Fine detection

Part B fine identification operates within the RoI provided by the faster R-CNN. The experimental procedure is shown in Fig. 7. It contains three steps: (B₁) self-correlation for center identification, (B₂) Intensity statistics for radii determination, and (B₃) calculation of excitation angle of SPs. Details of the three steps will be discussed in the following.

1) Self-correlation for center identification

According to the principle in Section II, the self-correlation enables to identify the center of axial symmetric shape or center symmetric shape in one step. This principle assumes that the pattern has only one center of symmetry, which requires a well-manufactured and well-assembled system configuration. In practical experiment, one needs to exclude the cases where the CA and SP profiles have different centers.

In this work, the centers of CA and SP profiles are identified respectively to see whether they are identical, as shown in Fig. 7(B₁). To identify centers with self-correlation, the CA and SP profiles on the BFP image should be separated first. The CA and SP profiles are separated by MET (minimum error thresholding) and RMET (radius-based minimum error thresholding) respectively [11, 23]. After that, the separated profiles are binarized, which is an inevitable requirement of self-correlation. 2-D convolution is conducted between the binarized image and its 180° rotation. The centers of CA and SP profile are determined according to the convolution results. Based on the principle from section II, centers are located at the maximum points of convoluted image. For most of the BFP images captured by our SPM, the two identified centers are nearly identical. One can take either of the two as the determined center of the BFP image. Several extreme cases where the centers of CA and SP profiles deviate from each other for more than 2 pixels are discarded to avoid severe measurement errors.

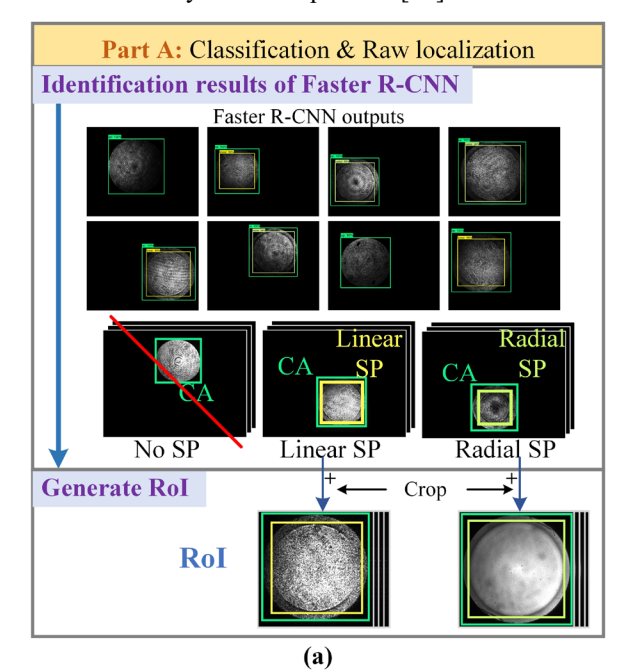
2) Intensity statistics for radii determination

In order to determine the radii of CA and SP profiles, the intensity statistics of the BFP image is calculated. Intensity statistics has two elements: center of intensity statistics, and interval of intensity statistics.

The center of intensity statistics is identical with the image center determined by self-correlation. The interval of intensity statistics is determined by the confidence interval of Faster R-CNN. To identify SP and CA profiles, the intensity statistics is conducted in the range of $r_{est} \pm 3\sigma_r$ (red region in Fig. 7(B₂)) and $R_{est} \pm 3\sigma_R$ (blue region in Fig. 7(B₂)) respectively. Intensity statistics curve is formed by evaluating radii in these ranges. Radius of SP profile is located at the radius with minimum intensity. And radius of CA profile is located at the radius with minimum difference.

3) Excitation angle

According to (5), excitation angle (EA) of SPs is determined by using the radii of SP and CA profiles. The measured excitation angles of different plasmonic samples are listed in TABLE V, which show a good consistence with the theoretical values calculated by Fresnel equations [24].



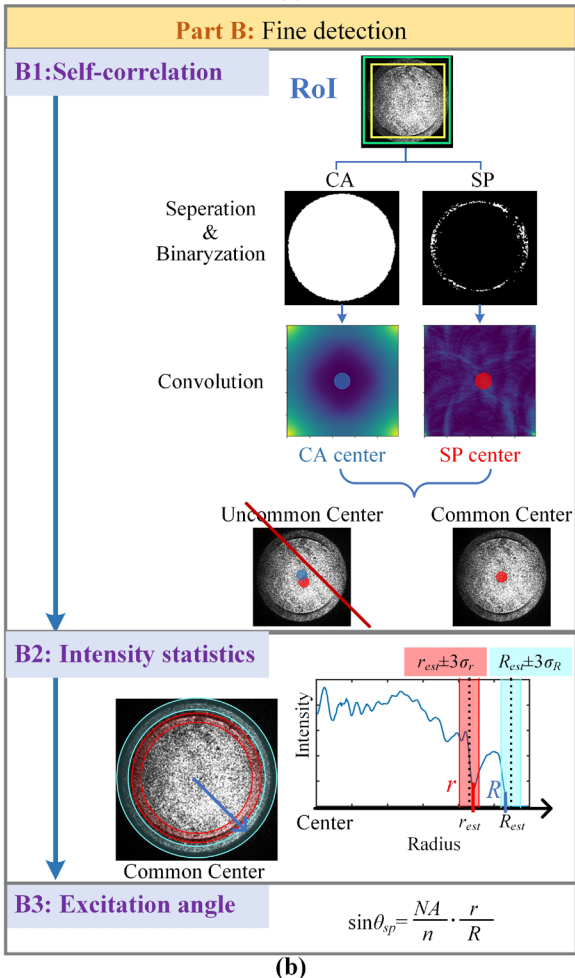


Fig. 7. Identification of SP and CA profiles has two parts. (a). Classification and Raw localization: The original outputs of Faster R-CNN in the experiment shows that Faster R-CNN achieves classification and localization. (b). Fine detection: B1: Separate SP and CA profiles and identify their respective centers. B2: Measure radii of SP and CA profiles on the intensity statistics curve. B3: Calculate excitation angle. The linear SP profile is taken as the example.

I ABLE V		
RESULTS OF	EXCITATION ANGLE	E MEASUREMENT

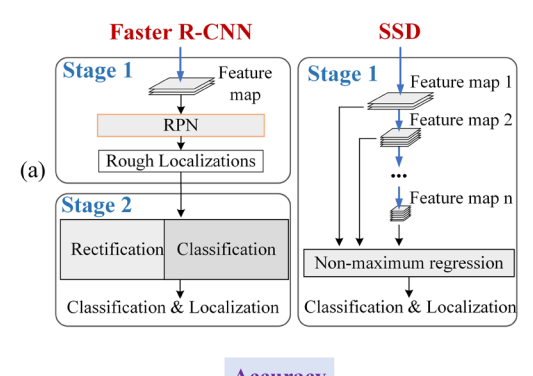
	5nm MgO	15nm MgO	20nm MgO
CA radius/Pixels	267	267	267
SP radius/Pixels	228	237	244
Measured excitation angle/degree	44.7	47.0	48.8
Theoretical excitation angle/degree	44.4	46.5	48.1

theoretical excitation angles are calculated by Fresnel equations.

V. DISCUSSIONS

In this section, the performances and advantages of the Faster R-CNN and self-correlation are discussed. More specifically, a quantitative comparison in procedure, accuracy, and speed is made between the Faster R-CNN and SSD, another object detection model. The advantages of self-correlation in universality and speed when compared with our previously proposed FCA is also illustrated.

A. Faster R-CNN versus SSD



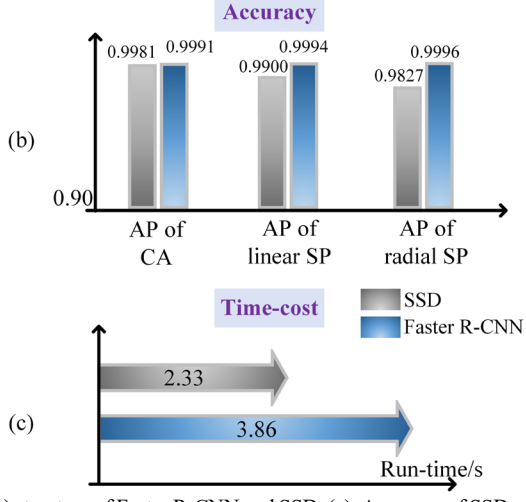


Fig. 8. (a) structure of Faster R-CNN and SSD. (a). Accuracy of SSD and Faster R-CNN in BFP-typed SPM (b). Time-cost of SSD and Faster R-CNN on an Intel(R) Core(TM) i5-6600 CPU.

Fig. 8 demonstrates the comparison between Faster R-CNN and SSD in principle (Fig. 8(a)), accuracy (Fig. 8(b)), and speed (Fig. 8(c)) respectively. As shown in Fig. 8(a), Faster R-CNN is a typical two-stage identification network. In stage 1, Faster R-CNN localizes the target object roughly by using RPN [15] which makes Faster R-CNN have better performance in speed

than many other two-stage identification networks, such as R-CNN [14] and Fast R-CNN [25]. In stage 2, the localization generated by RPN is rectified, and the target object is classified. By contrast, SSD [16] is a typical one-stage identification network. SSD extracts multiple feature maps of input image to classify and locate objects at the same time on all feature maps [16]. Final output is provided by non-maximum regression is SSD.

For a quantitative comparison between Faster R-CNN and SSD, the previous transfer learning approach (TABLE I) is utilized to transfer learn a pretrained SSD model [26] from TensorFlow 1 Detection Model Zoo. The model is also pretrained with the COCO dataset. For details of this model (training data, number of layers, etc.) readers can refer to [21, 26].

Fig. 8(b) shows the comparison in accuracy of the two networks. The term AP is utilized as the criterion. One can see that the Faster R-CNN is always more accurate than SSD. And this advantage of Faster R-CNN become more obvious when the identified SP profiles are in radial mode. Fig. 8(c) shows the time-cost of the two networks for identification of images obtained from the home-developed SPM. The identification is operated on Intel(R) Core(TM) i5-6600 CPU. It shows that the SSD is faster than Faster R-CNN.

The comparison results of the two networks are listed in TABLE VI. Faster R-CNN operates slower but with higher accuracy. This is because the second stage of Faster R-CNN offers correction of localization provided by the first stage, making identification more accurate but slower. Since the identification accuracy is much more essential in micro-Nano detection, Faster R-CNN is chosen in the experiment.

TABLE VI PERFORMANCE OF SSD AND FASTER R-CNN

	SSD	Faster R-CNN
Accuracy Time-cost	lower faster	Higher slower

B. Self-correlation versus FCA

Fig. 9 shows that the proposed self-correlation method has two advantage over the previously proposed FCA.

First, FCA may become ineffective in center identification of linear SP profile. The case is shown in Fig. 9(a₁). FCA convolutes original profile with horizontally/vertically flipped profile and use maximum of correlation coefficient to determine the horizontal/vertical location of the center of SP profile [12]. However, when the centers of the original profile and the flipped profile coincide, correlation-coefficient is always zero. In this case, one cannot figure out the location of the profile center. By contrast, self-correlation is applicable to center identification of all kinds of profiles including CA profile, linear SP profile, and radial SP profile. When the SP profile is in linear mode, self-convolution is still able to find the maximum of the correlation-coefficient (a₂).

Second, self-correlation determines center faster than FCA. In FCA, two convolution operations are required to determine the horizontal and vertical coordinates of the center respectively.

[6]

[15]

By contrast, self-correlation only utilizes one convolution operation to determine the center location. Fig. 9. (b) is a comparison of FCA and self-correlation in time-cost when applied to separated and binarized profiles. Both of them operate on Intel(R) Core (TM) i5-6600 CPU. The result shows an obvious advantage of self-correlation in calculation speed. When the mode of plasmonic signal is determined, the self-correlation procedure can operate independently, which means an extremely fast identification process.

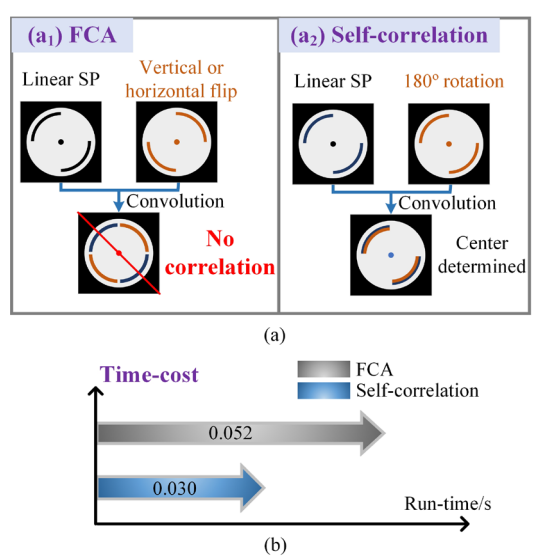


Fig. 9. (a₁). How FCA cannot be used to identify linear SP placed in a certain location. (a₂). Application of self-correlation to identify the linear SP which FCA cannot identify. (b). Average time-cost of FCA and Self-correlation. Measurement of time-cost is conducted with an Intel(R) Core(TM) i5-6600 CPU.

VI. CONCLUSION

In this work, a complete and feasible solution to identify BFP absorption profile was proposed and applied to excitation angle measurement. Both principle and experimental verification of the proposed solution were provided. Furthermore, the Faster R-CNN was shown to be more accurate than SSD despite relatively slower calculation speed. Self-correlation was also demonstrated to be more universal and faster than the previous FCA. To the best knowledge of the authors, this is the first time to present such a complete, automatic, and accurate solution for signal extraction of BFP typed SPM. This work greatly promotes the application and instrumentation of BFP typed SPM. It is worth noting that the object detection model in this work is a trial and mainly aims to verify the proposed complete identification scheme. In future works, other specific models can also be applied for the identification of BFP images.

we have uploaded all the data and codes to the submission system for the readers to reproduce the algorithm. The complete identification scheme in this work will be available at http://ieeexplore.ieee.org, which includes test images and Python executables (206MB)

[1] M. Bocková, J. Slabý, T. Špringer, and J. Homola, "Advances in surface plasmon resonance imaging and microscopy and their biological applications," *Annu. Rev. Anal. Chem.*, vol. 12, pp. 151-176, 2019. [2] S. Rampazzi, G. Danese, F. Leporati, and F. Marabelli, "A localized surface plasmon resonance-based portable instrument for quick onsite biomolecular detection," *IEEE Trans. Instrum. Meas.*, vol. 65, no. 2, pp. 317-327, 2015.

- [3] H. Kano, S. Mizuguchi, and S. Kawata, "Excitation of surface-plasmon polaritons by a focused laser beam," *J. Opt. Soc. Am. B.*, vol. 15, no. 4, pp. 1381-1386, 1998.
- [4] K. Moh, X.-C. Yuan, J. Bu, S. Zhu, and B. Z. J. O. l. Gao, "Radial polarization induced surface plasmon virtual probe for two-photon fluorescence microscopy," *Opt. Lett.*, vol. 34, no. 7, pp. 971-973, 2009
- [5] H.-M. Tan, "High resolution angle-scanning widefield surface plasmon resonance imaging and its application to bio-molecular interactions," University of Nottingham, 2011.
 - H.-M. Tan, S. Pechprasarn, J. Zhang, M. C. Pitter, and M. G. J. S. r. Somekh, "High resolution quantitative angle-scanning widefield surface plasmon microscopy," *Sci. Rep.*, vol. 6, p. 20195, 2016.
- [7] J. Zhang, C. See, and M. J. A. o. Somekh, "Imaging performance of widefield solid immersion lens microscopy," *Appl. Optics*, vol. 46, no. 20, pp. 4202-4208, 2007.
- [8] B. Huang, F. Yu, and R. N. Zare, "Surface plasmon resonance imaging using a high numerical aperture microscope objective," *Anal. Chem.*, vol. 79, no. 7, pp. 2979-2983, 2007.
- [9] S.-F. J. L.-Z. Hsieh, L.-B. Chang, C.-C. Hsieh, and C.-M. Wu, "Heterodyne interferometric surface plasmon resonance biosensor," *J. Med. Biol. Eng.*, vol. 26, no. 4, pp. 149-153, 2006.
- [10] B. Zhang, "Measuring plasmonic phase using radially polarized confocal surface plasmon interferometer," *IEEE Trans. Instrum. Meas.*, vol. 69, no. 10, pp. 7781-7786, 2020.
- [11] B. Zhang, C. Zhang, Q. Wang, P. Yan, and J. J. I. P. J. Wang, "Identification of plasmonic absorption profile in surface plasmon microscopy using morphology," *IEEE Photonics J.*, vol. 10, no. 6, pp. 1-9, 2018.
- [12] B. Zhang, Q. Wang, A. Li, and X. J. I. P. J. Wang, "Direct and Practical Identification for Back Focal Plane Based Surface Plasmon Microscopy," *IEEE Photonics J.*, vol. 12, no. 1, pp. 1-8, 2019.
- Z. Zou, Z. Shi, Y. Guo, and J. Ye, "Object detection in 20 years: A survey," arXiv preprint arXiv:1905.05055, 2019.
 R. Girshick, J. Donahue, T. Darrell, and J. Malik, "Rich feature
 - R. Girshick, J. Donahue, T. Darrell, and J. Malik, "Rich feature hierarchies for accurate object detection and semantic segmentation," in CVPR, Columbus, Ohio, USA, 2014, pp. 580-587. S. Ren, K. He, R. Girshick, and J. Sun, "Faster r-cnn: Towards real-time object detection with region proposal networks," in Adv. Neural. Inf. Process. Syst., Montreal, Quebec, Canada, 2015, pp. 91-
- [16] W. Liu et al., "Ssd: Single shot multibox detector," in ECCV, Amsterdam, Netherland, 2016: Springer, pp. 21-37.
- [17] B. Zhang and T. J. O. I. Xiao, "Avenue for apertometer using spectral plane and Fourier correlation analysis," *Opt. Lett.*, vol. 44, no. 17, pp. 4315-4318, 2019.
- [18] TensorFlow. Module: tf.keras.preprocessing.image | TensorFlow Core v2.4.1 [Online] Available: https://tensorflow.google.cn/api_docs/python/tf/keras/preprocessing/image
- [19] S. J. Pan and Q. Yang, "A survey on transfer learning," *IEEE Trans. Knowl. Data. Eng.*, vol. 22, no. 10, pp. 1345-1359, 2009.
- [20] Tensorflow.org. faster_rcnn_inception_v2_coco [Online] Available: http://download.tensorflow.org/models/object_detection/faster_rcn_n_inception_v2_coco_2018_01_28.tar.gz
- [21] Tensorflow.org. TensorFlow 1 Detection Model Zoo [Online] Available:
 - https://github.com/tensorflow/models/blob/master/research/object_detection/g3doc/tfl_detection_zoo.md
- [22] M. J. D. o. S. Zhu and U. o. W. Actuarial Science, Waterloo, "Recall, precision and average precision," vol. 2, p. 30, 2004.
- [23] J. Kittler and J. Illingworth, "Minimum error thresholding," *Pattern. Recognit.*, vol. 19, no. 1, pp. 41-47, 1986.
- [24] A. W. Peterson, M. Halter, A. L. Plant, and J. T. J. R. o. S. I. Elliott, "Surface plasmon resonance microscopy: Achieving a quantitative optical response," *Rev. Sci. Instrum.*, vol. 87, no. 9, p. 093703, 2016.
 [25] R. Girshick, "Fast r-cnn," in *ICCV*, Santiago, Chile, 2015, pp. 1440-
- [26] Tensorflow.org. ssd_mobilenet_v1_coco [Online] Available: http://download.tensorflow.org/models/object_detection/ssd_mobilenet_v1_coco_2018_01_28.tar.gz